Renewable Energy 197 (2022) 564–573

Contents lists available at ScienceDirect

Renewable Energy

journal homepage: www.elsevier.com/locate/renene

Influence of element substitution on structural stability and hydrogen storage performance: A theoretical and experimental study on $TiCr_{2-x}Mn_x$ alloy

Wenbin Jiang [a,1], Changchun He [b,1], Xiaobao Yang [b,**], Xuezhang Xiao [c,***], Liuzhang Ouyang [a,d,*], Min Zhu [a]

[a] School of Materials Science and Engineering and Key Laboratory of Advanced Energy Storage Materials of Guangdong Province, South China University of Technology, Guangzhou, 510641, People's Republic of China

[b] Department of Physics, South China University of Technology, Guangzhou, 510641, People's Republic of China

[c] State Key Laboratory of Silicon Materials, School of Materials Science and Engineering, Zhejiang University, Hangzhou, 310027, People's Republic of China

[d] China-Australia Joint Laboratory for Energy & Environmental Materials and Key Laboratory of Fuel Cell Technology of Guangdong Province, Guangzhou, 510641, People's Republic of China

A R T I C L E I N F O

Keywords:
$TiCr_{2-x}Mn_x$ alloy
Structural stability
Hydrogen storage properties
First-principles

A B S T R A C T

AB_2-type alloys have been widely used for metal hydride hydrogen compressors and hydrogen storage systems. The crystal structure and hydrogen storage properties mostly rely on their composition and atomic distribution. Thus, revealing the relationship between structure and properties can lead to the design of alloys with optimized properties for hydrogen storage application. Here, the structure stability, bonding energy, thermodynamic and kinetic properties of $TiCr_{2-x}Mn_x$ (x = 0, 0.25, 0.5, 0.75, 1) alloy/hydride have been firstly investigated by combining density functional theory calculation and experiment. It demonstrates that Mn-doped $TiCr_2$ alloy has a stable C14 phase, and Mn can optionally substitute for Cr sites. Additionally, with increase of Mn content, the desorption plateau increases and the ΔH value decreases. In particular, the ΔH values of $TiCr_{2-x}Mn_x$ hydrides are consistent with the heat released when H atoms occupy the interstitial interstices. Finally, the hydrogen absorption kinetics simulation shows that Mn is unfavorable to the hydrogen absorption kinetics, in which TiCrMn is 124 s longer than $TiCr_2$ when 90% hydrogen-absorption capacity is reached. The relationship between calculations and experiments presents here can be used as a reference for subsequent screening of alloying elements with high melting point and cost for metal hydride system.

1. Introduction

Hydrogen is a clean, renewable, high energy efficiency and promising green energy carrier for future development [1–5]. Metal hydrides (MHs), such as hydrogen compression materials and solid-state hydrogen storage materials, are strategic materials for the extensive use of hydrogen-based energy systems [6–9]. However, there are only a few of alloys, including TiCr-base [10–12] and ZrFe-base [13,14] AB_2-type alloy, can be developed as the candidates. With the increasing requirements for high hydrogen storage capacity, low hysteresis and suitable plateau pressure, especially those serving at room temperature to 80 °C [15]. TiCr-base AB_2-type alloys show the best potential due to their wide plateau, high hydrogen storage capacity and stable phase structure [16], as well as the low cost. However, the original $TiCr_2$ alloy cannot be used as hydrogen compression material due to its low capacity and high slope. Therefore, a lot of studies [17], both experimental and theoretical, have been carried out on element substitution of $TiCr_2$ alloy.

In order to avoid the formation of two temperature-dependent allotropes of original $TiCr_2$ alloy, Beeri et al. [18,19] attempted to substitute Mn for some of Cr and succeeded in obtaining a single-plateau TiCrMn

* Corresponding author. School of Materials Science and Engineering and Key Laboratory of Advanced Energy Storage Materials of Guangdong Province, South China University of Technology, Guangzhou, 510641, People's Republic of China.
** Corresponding author.
*** Corresponding author.
E-mail addresses: scxbyang@scut.edu.cn (X. Yang), xzxiao@zju.edu.cn (X. Xiao), meouyang@scut.edu.cn (L. Ouyang).

[1] These authors contributed equally to this work.

https://doi.org/10.1016/j.renene.2022.07.113
Received 27 March 2022; Received in revised form 10 July 2022; Accepted 21 July 2022
Available online 6 August 2022

alloy. Similarly, Bruzzone et al. [20] obtained single-phase C14 structure alloy by substitution Cr with Fe. The thermodynamic stability of $TiCr_{1.94-x}Fe_x$ hydride decreases with the Fe addition. Furthermore, more alloying references of $TiCr_2$-base alloys are summarized in Supplementary Materials Table S1.

Alloying with transition elements to improve the comprehensive properties of the original alloy is effective but time-consuming. Computational tools for predicting phase structure and hydrogen storage properties are essential to efficiently navigate in the endless sea of compositions available. Nong et al. [21] confirmed that Mn atoms can optionally substitute on the Cr sites of $TiCr_2$ alloy by the first-principles calculations and successfully predicted the hydrogen storage performance of ternary intermetallic TiCrMn. Furthermore, Li et al. [22] reported that partial substitution Cr with transition metal Fe in $TiCr_2$ leads to a decrease in the hydrogen absorption/desorption kinetics, while V leads to an increase in the hydrogen absorption/desorption kinetics.

Unfortunately, despite considerable experimental and theoretical studies on $TiCr_2$-base alloy, there are still barely able to provide a thorough illumination for the relationship of how components and atomic distribution of the alloying elements affect the structure and hydrogen storage properties of the host binary metals. Moreover, the kinetics of dissociation of H_2 on the surface and the diffusion of H atom in the bulk alloy also play important roles in determining the application of $TiCr_2$-base alloys.

Here, we perform the first-principles calculations and corresponding experimental investigations to clarify the relationship of components and atomic distribution on structure stability and the hydrogen storage behaviors of Mn-doped $TiCr_2$ alloy. The present studies show that the crystal structure and hydrogen storage properties of $TiCr_{2-x}Mn_x$ alloys both in theory and experiment are in good agreement. In addition, the effect of Mn addition on the kinetics of $TiCr_{2-x}Mn_x$ alloys were also revealed theoretically.

2. Methods

2.1. Computational details

All calculations of $TiCr_{2-x}Mn_x$ (x = 0, 0.25, 0.5, 0.75, 1) alloys and their hydride were performed using the Vienna *ab* initio simulation package (VASP), where the projector-augmented wave (PAW) method was adopt within the Perdew-Burke-Ernzerhof generalized gradient approximation (GGA) for the exchange-correlation functional [23,24]. A cutoff energy of 500 eV and a k-points mesh with 9 × 9 × 6 were applied. For all alloy structures, the spin polarized calculations were considered. In addition, the structural relaxation was fully conducted until the energy difference tolerance and the total force were less than 1×10^{-6} eV atom^{-1} and 0.01 eV Å^{-1}, respectively. In order to deal with the 3*d* electron–electron correlation [25], GGA + U type calculations are carried out during structural optimization. And the values of Hubbard U parameter of Ti, Cr and Mn were tested and fixed at 2.96, 2.97 and 3.19 eV, respectively. Climbing image nudged elastic-band (CI-NEB) method was employed to calculate the H_2 dissociation and H atom diffusion barriers during the hydrogen absorption/desorption process.

Here, the surface energy E_{surf} of the slab model is defined as [26,27]:

$$E_{surf} = \frac{1}{2A}\left(E_S^{unrelax} - NE_b\right) + \frac{1}{A}\left(E_S^{relax} + E_S^{unrelax}\right) \tag{1}$$

where A is surface area of the cleaved surface, $E_S^{unrelax}$ and E_S^{relax} are the total energy of the slab model before and after relaxation, N presents the number of the unite in the slab, E_b is the bulk energy per unite.

The adsorption energy E_{ads} of H atom on the alloy surface is calculated as follows [28,29]:

$$E_{ads} = \frac{1}{N}\left(E_{slab-N(H)} - E_{slab} - NE_H\right) \tag{2}$$

where N is the number H atoms, $E_{slab-N(H)}$ is the total energy of the slab structure with H atom. E_{slab} are the total energy of the slab structure without H atom, E_H is the total energy of free H atom.

2.2. Experimental

The $TiCr_{2-x}Mn_x$ (x = 0, 0.25, 0.5, 0.75, 1) alloys weighted 15g for each ingot were prepared by non-consumable vacuum arc furnace. Before melting, the Mn pieces were sealed in a quartz tube of 10^{-3} Pa and then annealed at 900 °C for 20 h to remove the oxide layer. After melting, the ingots were annealed at 850 °C for 10 h to eliminate internal stresses and lattice defects [30]. The crystal structures were determined by X-ray diffraction (PANalytical Empyrean with Cu Kα radiation) and the cell parameters were obtained by Rietveld refinement using GSAS software [31]. The morphologies and elemental contents of these alloys were observed using scanning electron microscopy (SEM, Zeiss Supra 40/VP) with an energy dispersive X-ray spectrometer (EDS, Oxford INCA).

The hydrogen storage properties were tested on a high-pressure pressure-composition-temperature system from 0 to 40 MPa under a temperature range of 10–70 °C. Before testing, all alloys were activated completely under 40 MPa at −20 °C for 8 h, and then the kinetics of the first hydrogen absorption was tested under 30 MPa at 30 °C.

3. Results and discussion

3.1. Structural stability and characterization

The $TiCr_2$ alloy of C14-type possess a hexagonal structure, and the cell molecular formula is Ti_4Cr_8 [32], as shown in Fig. 1 (a). The original structure parameters for density functional theory (DFT) calculation of $TiCr_2$ ($a = 4.877$ Å, $c = 7.868$ Å and $V = 162.05$ Å^3) draw on the work by Svechnikov et al. [33]. The Mn atoms were considered to optionally substitute for the Cr sites of $TiCr_2$ to form the ternary intermetallic $TiCr_{2-x}Mn_x$ [21]. Therefore, the total number of possible structures composed of $Ti_4Cr_{8-x}Mn_x$ is 2^8 dues to the alternative Cr atoms within the primitive cell is 8. In practice, however, 38 identical structures were obtained after removing the equivalent structures by the structural recognition [34,35]. The stability of the obtained structures can be determined by the formation enthalpy E_f. A negative formation enthalpy indicates a high stability of the obtained structures and E_f for a given structure $AB_{2-x}M_x$ (M = substitution metal) can be defined as [34, 36–38]:

$$E_f = E_t - (1-x) \times E_{AB_2} - xE_{AM_2} \tag{3}$$

where E_t, E_{AB_2} and E_{AM_2} are, respectively, the total energy of the given structure, the end-point solids AB_2 and AM_2, x is the ratio of variable M atoms to their sum. The calculated E_f for these 38 cells of $TiCr_{2-x}Mn_x$ alloys are showed in Fig. 1 (b). All the substituted structures possess the negative formation enthalpies, indicating that all substituted structures for certain stoichiometry are stable. Again, these show that Mn atoms can optionally substitute for the Cr sites of $TiCr_2$ alloy [21]. Furthermore, the structures of Mn substitute for Cr with the lowest E_f for each stoichiometry from x = 0 to 1 exhibit ordered substitution in order of fractional coordinates (1, 0, 0.5), (1, 0, 1), (0.83, 0.17, 0.25), (0.17, 0.83, 0.75), as shown in Fig. 1 (a). However, it is worth noting that Cr and Mn are actually disordered substitutions in $TiCr_{2-x}Mn_x$ alloys, because it's not possible to separate Cr and Mn atoms by using X-ray scattering.

The crystal structure of $TiCr_{2-x}Mn_x$ (x = 0, 0.25, 0.5, 0.75, 1) alloys are further confirmed by XRD analysis using the as cast alloys, as shown in Fig. 1 (c). There is only a single C14 Laves phase in $TiCr_{2-x}Mn_x$ alloys with hexagonal $MgZn_2$-type structure. The results of the backscattered electron images, elemental mappings and EDS analysis, as shown in Supplementary Materials Fig. S1 and Table S2, further confirm this

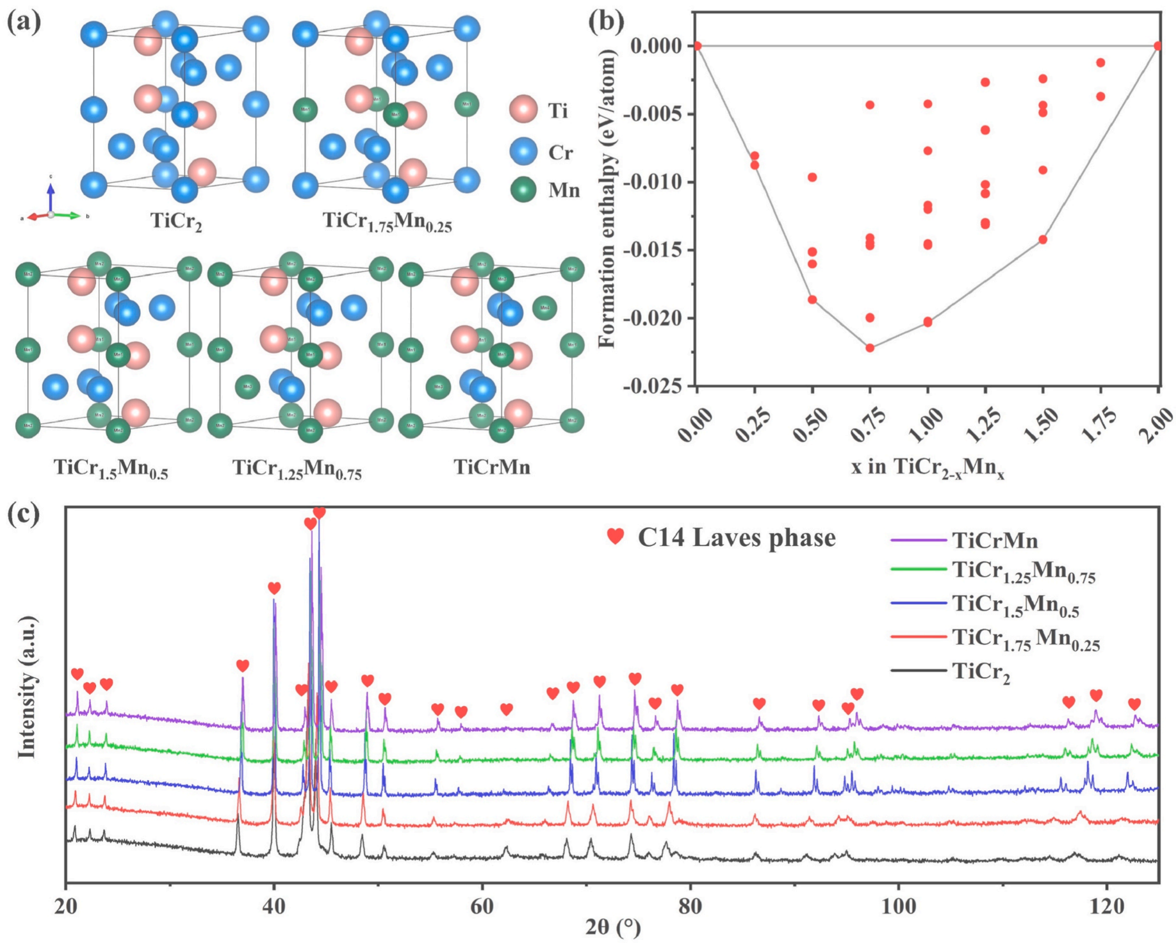

Fig. 1. The structure stability of $TiCr_{2-x}Mn_x$ alloys: the site of Mn substituted for Cr in $TiCr_{2-x}Mn_x$ alloy in DFT (a), formation enthalpy (b) and XRD patterns of $TiCr_{2-x}Mn_x$ annealed alloys (c).

single-phase structure, which is in good consistency with the phase structure predicted by formation enthalpy analysis. The elemental compositions analysis of these alloys agree well with the desired compositions. In addition, the lattice constants *a*, *c* and cell volumes *V* of annealed alloys are derived from Rietveld refinement, as shown in Fig. S2 and Table 1. As seen, *a* is sensibly reduced by substitution of Cr by Mn. While, unlike the results of Agresti et al. [39] that *c* remains almost unchanged in $TiCr_{1.78-x}Mn_x$ alloys. Here, the *c* increases firstly from 7.9885 Å for $TiCr_2$ to 7.9913 Å for $TiCr_{1.5}Mn_{0.5}$ then decreases to 7.9672 Å for TiCrMn, which have a good agreement with the same compositions alloys ($TiCr_{2-x}Mn_x$ (x = 0.5, 0.75, 1)) reported by O. Beeri et al. [18]. The lattice constants obtained from structure optimization are in good agreement with the experimental results and the deviation of lattice constants *V* is within 0.4%.

Table 1
The calculated and experimental lattice parameters of $TiCr_{2-x}Mn_x$ alloys.

Alloy	Lattice constants (calculated)			Lattice constants (annealed)		
	a/Å	c/Å	Volume V/Å^3	a/Å	c/Å	Volume V/Å^3
$TiCr_2$	4.9179	7.9981	167.52	4.9109 (4)	7.9885 (1)	166.85 (3)
$TiCr_{1.75}Mn_{0.25}$	4.9014	7.9554	165.51	4.8987 (1)	7.9897 (1)	165.92 (1)
$TiCr_{1.5}Mn_{0.5}$	4.8982	7.8987	164.12	4.8762 (1)	7.9913 (1)	164.55 (1)
$TiCr_{1.25}Mn_{0.75}$	4.8998	7.8696	163.62	4.8640 (1)	7.9812 (1)	163.53 (1)
TiCrMn	4.8987	7.8533	162.21	4.8550 (1)	7.9672 (1)	162.64 (1)

3.2. Electronic structure

3.2.1. Electronic properties

The interaction between doped atoms and interstitial atoms is necessary to be clarified for the study of the hydrogen storage behavior of alloys. The addition of Mn not only causes the lattice distortion, but also affect the chemical interactions between atoms to some extent. And the essence of the change in chemical interactions around the interstitial atoms is a change in the electron structure. Fig. 2 (a) and (d) shows the total density of states (TDOS) of the most stable structures based on the formation enthalpy analysis of $TiCr_{2-x}Mn_x$ alloy. The calculated results reveal that $TiCr_{2-x}Mn_x$ and $TiCr_{2-x}Mn_x$-H exhibit obvious metallic behavior because of the large states near the Fermi surface. Furthermore, a notable difference between $TiCr_{2-x}Mn_x$ from x = 0 to 1 is that the TDOS shift appreciably to low energy with the increase of the Mn content. Obviously, the $TiCr_{2-x}Mn_x$ system becomes less stable in structure stabilities after the addition of Mn [40]. Additionally, as shown in Fig. 2 (b–c) and (e-f), with the addition of Mn atoms, the *d*–orbital hybridization among Ti, Cr and Mn obviously lead to an enhancement in the strength to metal bond, implying that charges are involved in the hybridization. And the strong chemical interaction between the H atoms and Ti/Cr/Mn atoms, which directly affects the diffusion and dissolution of the H atoms in $TiCr_{2-x}Mn_x$ of alloys.

Furthermore, the charge density distribution of the $TiCr_{2-x}Mn_x$-H system is also conducted by adding a H atom to the A_2B_2 tetrahedral

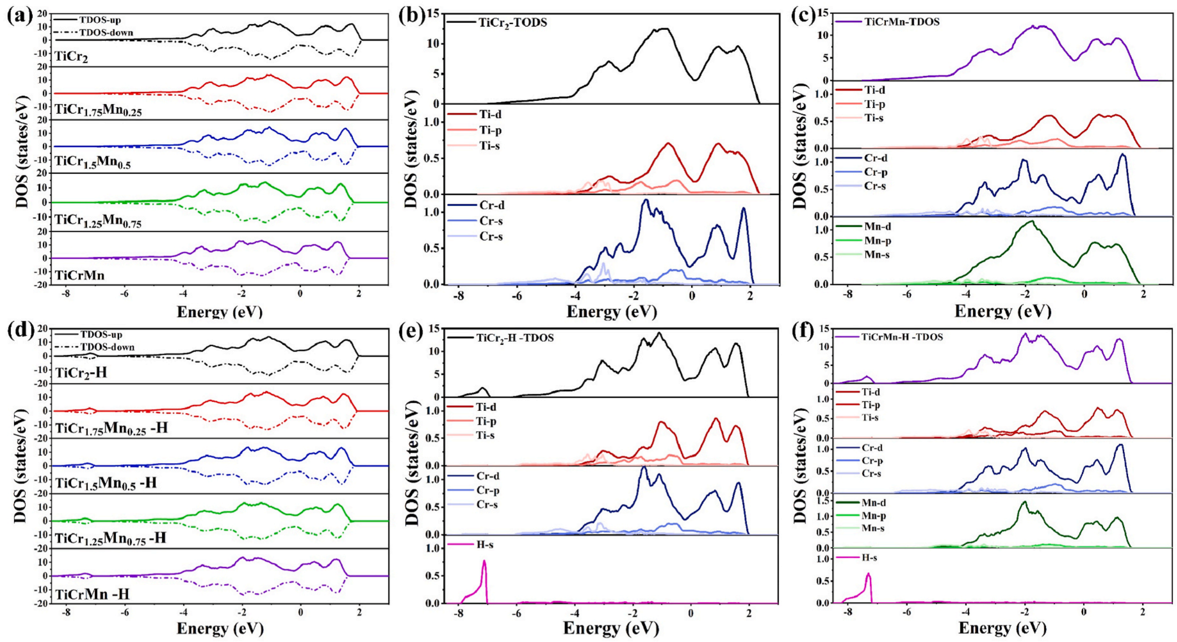

Fig. 2. Total and partial DOS of the most stable structure of $TiCr_{2\text{-}x}Mn_x$ and $TiCr_{2\text{-}x}Mn_x$-H system.

interstice as shown in Fig. 3. There are strong directional bonds between H atom and neighbor Cr/Mn atom. Compared with the Cr–H bond (1.71 Å), the bond length of Mn–H bond (1.66 Å) is shorter. It indicates again that stronger interactions existing between H and Mn atoms compare with H and Cr atoms, which further confirms the results of the alloys and hydrides in DOS analysis.

3.2.2. Bonding energy model

To quantify the bonding energy between the atomic pair in the $TiCr_{2\text{-}x}Mn_x$ ($x = 0, 0.25, 0.5, 0.75, 1$) alloy/hydride, a first-neighbor bond energy model (BEM) is introduced, based on the total energy of given substituted structures. The expression of BEM is given as below [41]:

$$E_{BEM} = \sum n_{ii}J_{ii} + \sum n_{jj}J_{jj} + \sum n_{kk}J_{kk} + \sum n_{ll}J_{ll} + \sum n_{ij}J_{ij}\cdots \tag{4}$$

Where n_{ii}, n_{jj}, n_{kk}, n_{ll}, n_{ij}, ⋯ are the total number of these first-neighbor Ti–Ti, Cr–Cr, Mn–Mn, H–H, Ti–Cr, …bonds (i, j, k, l = Ti, Cr, Mn, H) in all alloy crystal, J_{ii}, J_{jj}, J_{kk}, J_{ll}, J_{ij} ⋯ are the bond energy of these bonds, respectively. Here, total energy of alloy is divided among these first-neighbor bonds. Hence, there are 38 substituted structures (**see in Section 3.1**) of $TiCr_{2\text{-}x}Mn_x$ alloy to fit the parameters in BEM, as shown in Fig. 4. There is a linear dependence of the calculated total energies from DFT (E_{DFT}) on those from BEM (E_{BEM}), indicates the total energies of $TiCr_{2\text{-}x}Mn_x$ and $TiCr_{2\text{-}x}Mn_x$ –H system can be well described by the bond energy model. It is important to bear in mind that the BEM intends only to find reasonable values for relative bond energy and not an accurate description of the bond energy of $TiCr_{2\text{-}x}Mn_x$ alloys and hydrides. As a result, Ti–Mn bond is positive with 0.0097 eV, while Ti–Cr bond is negative with −0.0125 eV, indicates the total energy of $TiCr_{2\text{-}x}Mn_x$ system will shift to a positive value. In addition, the comparison of Cr–H bond (0.0220 eV) and Mn–H bond (0.0310 eV) shows that, similarly, the addition of Mn causes the MHs structure to become less stable than that of $TiCr_2$. It is possible that the thermodynamic stability of $TiCr_{2\text{-}x}Mn_x$ hydrides from x = 0 to 1 will gradually decrease.

3.3. Hydrogen storage properties

3.3.1. Hydrogen storage behavior in DFT

Most potential AB_2-type alloy with the ideal stoichiometric crystallize as the hexagonal $MgZn_2$ (C14), cubic $MgCu_2$ (C15) or less frequently $MgNi_2$ (C36) Laves phase [8]. $TiCr_{2\text{-}x}Mn_x$ ($x = 0, 0.25, 0.5, 0.75, 1$) alloys are confirmed to be C14 Lave phase, with four formula units per unit cell. And the hydrogen atoms in MHs may occupy one or more of three types of tetrahedral interstices, including A_2B_2-, AB_3- and B_4-type tetrahedral interstice, as shown in Fig. S3 and Table S3. There are in total of 17 such interstices per AB_2 formula unit, i.e. 12 A_2B_2, 4 AB_3 and 1 B_4 interstices. However, most of the interstices remain unoccupied during hydriding due to the electrostatic effects, resulting in a maximum hydrogen storage capacity of about 6 H atoms per AB_2 formula unit [42, 43]. In addition, according to Shoemaker's exclusion rule [44], these H atoms in both cases should be excluded. One case, the distance between the faces of tetrahedral interstices to the centre of tetrahedral interstices

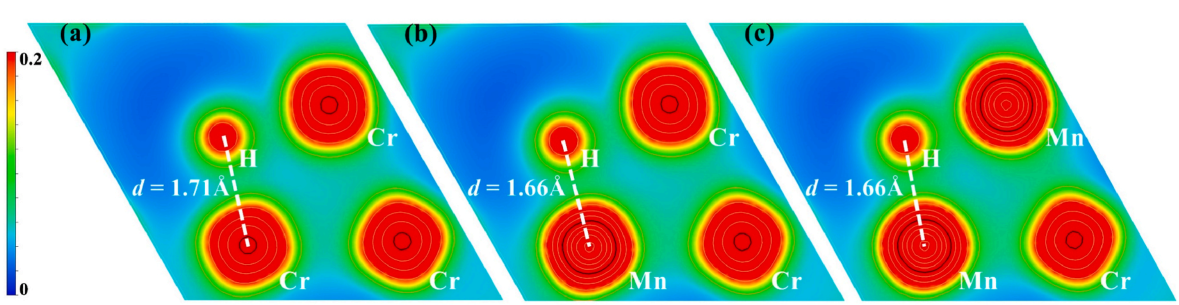

Fig. 3. Charge densities of A_2B_2 tetrahedral interstices of $TiCr_{2\text{-}x}Mn_x$-H alloys: Ti–Ti–Cr–Cr interstice (a), Ti–Ti–Cr–Mn interstice (b), Ti–Ti–Mn–Mn interstice (c).

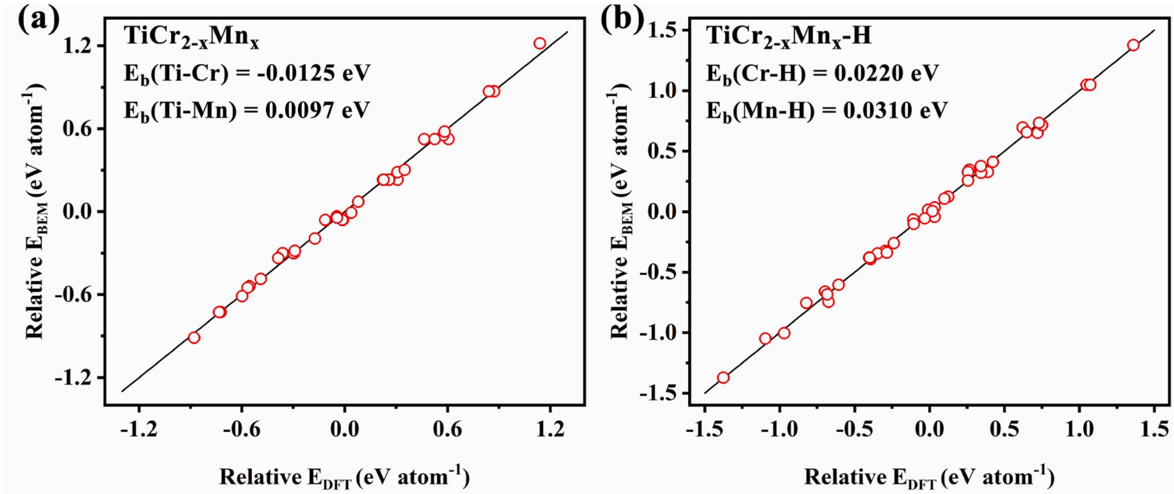

Fig. 4. Total energies of $TiCr_{2-x}Mn_x$ and $TiCr_{2-x}Mn_x$-H systems obtained by DFT calculation and by BEM method (red circle).

is less than 1.6 Å, which is below the limiting H–H internuclear distance of 2.1 Å for hydrides proposed by Switendick [45]; the other case, two tetrahedral interstices having a triangular face in common may not both accommodate H atom at their centers. Thereby, the actual hydrogen storage capacity of AB_2 is lower than that of AB_2H_6.

Here, in order to illustrate the ease with which the alloys absorb hydrogen, one H atom was added to each of the three types of tetrahedral interstices mentioned above, and the solution enthalpy E_{sol} of the interstitial H atom in bulk alloy can be obtained as [40,46]:

$$E_{sol} = E_{bulk+H} - E_{bulk} - \frac{1}{2}E_{H_2} \quad (5)$$

where E_{bulk+H} and E_{bulk} are the total energies of the bulk with H atom and without H atom, respectively. E_{H_2} is the total energy of H_2. As summarized in Table 2, a negative E_{sol} denotes an exothermic reaction; a lower E_{sol} means that the tetrahedral interstice is easier to absorb hydrogen, which is reflected in lower plateau pressure in PCT. The values of E_{sol} are negative for all A_2B_2 tetrahedral interstices. Among them, the $6h_1$ tetrahedral interstice represents the lowest E_{sol} with −0.1881 eV, indicating that $6h_1$ tetrahedral interstice is the most easily occupied by H atom. It's worth noting that the E_{sol} of AB_3-type and B_4-type tetrahedral interstices are positive, imply that higher hydrogen pressures are required for H atoms to occupy these interstices during the hydrogen storage application [18]. The results of neutron diffraction result by Zhu et al. [47] and statistical thermodynamics analysis by Beeri et al. [18,19] also confirmed that H atoms preferentially occupied A_2B_2 tetrahedral sites in YFe_2-based alloy and $TiCr_{2-x}Mn_x$-H system. Additionally, the solution enthalpy of H atoms in hydride and bulk alloy were compared. As shown in Fig. S4, take the E_{sol} of H atoms at the 24l tetrahedral interstices as an example, the value of E_{sol} increases almost linearly from −0.25 eV for 2 H atoms to −0.96 eV for 8 H atoms in hydride. Obviously, the E_{sol} depends on the type of tetrahedral interstice rather than the concentration of H in the hydride in both alloys/hydrides.

Furthermore, the E_{sol} of H atom in the tetrahedral interstice with Mn-

Table 2
The solution enthalpy of H atom at different tetrahedral interstitial.

Tetrahedral interstice	type	E_{sol}/eV	E_{sol} (Mn-doped)/eV
A_2B_2	$6h_1$	−0.1881 (TiTiCrCr)	−0.0647 (TiTiCrMn)
	$6h_2$	−0.1028 (TiTiCrCr)	−0.0473 (TiTiCrMn)
	$12k_2$	−0.1077 (TiTiCrCr)	−0.0034 (TiTiCrMn)
	24l	−0.1405 (TiTiCrCr)	−0.0083 (TiTiCrMn)
AB_3	4f	0.1575 (TiCrCrCr)	0.1766 (TiCrCrMn)
	$12k_1$	0.0404 (TiCrCrCr)	0.0966 (TiCrCrMn)
B_4	4e	0.6576 (CrCrCrCr)	–

doped were calculated, also listed in Table 2. The E_{sol} values of Mn-doped alloy offset in a positive direction, indicate the desorption plateau pressure $TiCr_{2-x}Mn_x$ alloys will increase with the Mn addition. According to Miedema's equation [48–50], the derived reaction enthalpy (*ΔH*) of MHs will decrease with the addition of Mn due to the reduced of heat release when H atoms occupying tetrahedral interstitials.

3.3.2. Hydrogen storage behavior in experiments

Although the hydrogen storage properties of alloys are predicted by DFT method, they are difficult to quantify. Here, AB_2-type hydrogen storage alloys, which operation temperature is between room-temperature to 80 °C, have great application potential in stationary hydrogen compressor of hydrogen refueling station. To study the performance of $TiCr_{2-x}Mn_x$ alloys under working conditions, the PCI curves of the alloys were measured at 10, 30, 50 and 70 °C, as shown in Fig. 5. The hydrogen storage characteristics, including hydrogen desorption plateau pressure P_d, reversible hydrogen storage capacity C_{Re}, hysteresis factor H_f, plateau slope factor S_f, and the derived reaction enthalpy (*ΔH*) and entropy (*ΔS*), can be obtained from the PCT curves and summarized in Table 3. As shown in Fig. 5 (a-e), H_f and S_f [51] of original $TiCr_2$ alloy are unacceptable for the application requirement. With the substitution of Cr by Mn, H_f and S_f decrease firstly, the $TiCr_{1.5}Mn_{0.5}$ and $TiCr_{1.25}Mn_{0.75}$ alloys show the smallest H_f and S_f with 1.02 and 0.14, respectively. However, with the further increase Mn contents in $TiCr_{2-x}Mn_x$ alloys, the H_f and S_f began to deteriorate.

The reversible capacity C_{Re} can also be obtained from the PCT curves. The C_{Re} of $TiCr_2$ alloy are only 1.49 wt% on its first absorption/desorption plateau at 30 °C, which only the lower composition hydride phase (AB_2H_3 phase) was formed while the high-composition hydride phase (AB_2H_4 phase) was not formed [18]. With the substitution of Cr by Mn, the C_{Re} increases at first to 1.88 wt% for $TiCr_{1.5}Mn_{0.5}$ alloy, then decreases to 1.72 wt% for TiCrMn alloy at 30 °C. The same regular are found at 50 °C. The addition of Mn is beneficial to adjust the hydride phases and the plateau performance of the alloy [52,53], which can increase of the hydrogen storage capacity. However, the reduction of cell volumes prevents further increase of C_{Re}. Taken together, the maximum C_{Re} with 1.88 wt% is obtained at x = 0.5 in $TiCr_{2-x}Mn_x$ alloys.

Lastly, the hydrogen absorption/desorption plateau pressure is one of the most important characteristic of hydrogen compression materials, which can also obtain from the PCT curves. $TiCr_2$ alloy has been confirmed to exist on two hydrogen absorption/desorption plateau by Johnson et al. [16]. Here, due to the constraints of temperature and pressure, only one plateau can be reached, and the hydrogen storage

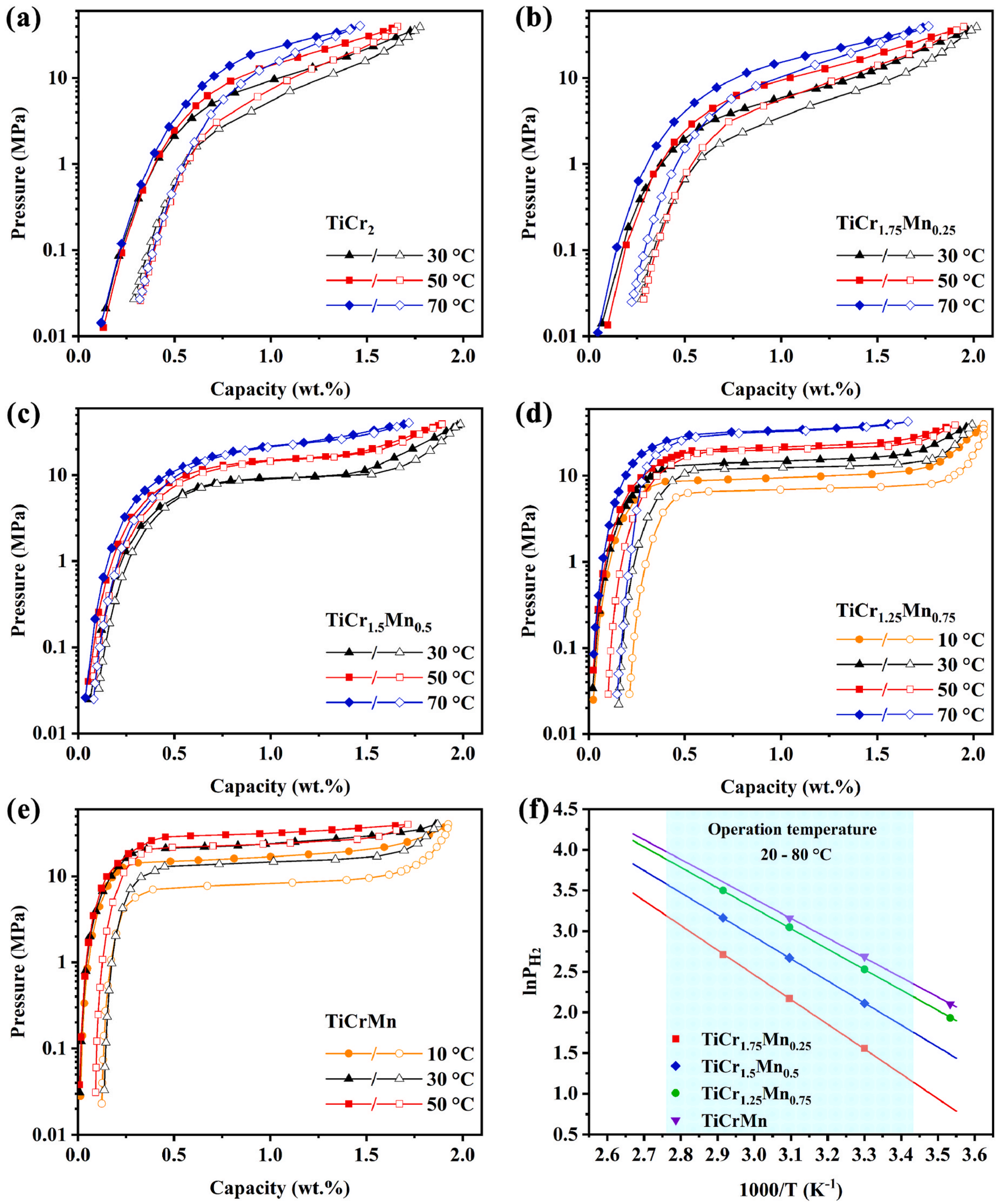

Fig. 5. Hydrogen absorption/desorption performance of $TiCr_{2\text{-}x}Mn_x$ alloys at 10, 30, 50 and 70 °C (a–e) and Van't Hoff plot (f).

Table 3
Hydrogen storage behavior of the $TiCr_{2\text{-}x}Mn_x$ alloys.

Sample	P_{de}/MPa				Desorption capacity/wt.%				ΔH/kJ/mol H_2	ΔS/J $mol^{-1}K^{-1}$	Ab. kinetics t/s
	10 °C	30 °C	50 °C	70 °C	10 °C	30 °C	50 °C	70 °C			
$TiCr_2$	–	4.45	6.85	9.69	–	1.49	1.34	1.15	–	–	36.7
$TiCr_{1.75}Mn_{0.25}$	–	4.69	6.96	10.19	–	1.74	1.67	1.54	24.88	95.11	57.6
$TiCr_{1.5}Mn_{0.5}$	–	9.16	14.43	19.77	–	1.88	1.81	1.64	22.77	92.68	70.6
$TiCr_{1.25}Mn_{0.75}$	7.05	12.52	20.14	33.10	1.84	1.83	1.80	1.51	21.20	90.98	78.1
TiCrMn	8.18	14.66	23.56	–	1.80	1.72	1.62	–	20.11	88.60	160.7

characteristics of $TiCr_2$ alloy here are only for a reference. According to the PCT curves, with the addition of Mn, the P_d monotonically increase from 4.45 MPa for $TiCr_2$ to 14.66 MPa for TiCrMn at 30 °C. Furthermore, the thermodynamic performance of the metal hydride can be fitted by Van't Hoff equation with hydrogen desorption plateau pressures [54, 55]:

$$\ln\frac{P_{de}}{P^{\theta}}=\frac{\Delta H}{RT}-\frac{\Delta S}{R} \tag{6}$$

where P^{θ}, P_{de}, T ΔH and ΔS respectively represent the standard pressure, the ideal gas constant, the absolute temperature (K), the changes in enthalpy and entropy of hydrogen desorption process. The ΔH and ΔS can be calculated by the slope and intercept of the fitting curves. As a result, in Table 3, the absolute values of ΔH and ΔS decrease with increasing Mn content from 24.88 kJ/mol H_2 and 95.11 J mol^{-1} K^{-1} for $TiCr_{1.75}Mn_{0.25}$–20.11 kJ/mol H_2 and 88.60 J mol^{-1} K^{-1} for TiCrMn, respectively, suggesting that the stability of the hydride ceaselessly reduce with the Mn addition. It is interesting that the change of ΔH is successfully predicted by the results of first-principles calculations.

3.3.3. Relationship between ΔH and E_{sol}

In addition to fitting the ΔH of AB_2 alloy with Van't Hoff formula, other formulas can be used to calculate the ΔH, of which Miedema's formula [42,48–50] is widely accepted. According to Miedema's formula, the value of ΔH is calculated from summing the heats of formation of the imaginary binary hydrides formed by each atom around the interstice. The calculation of ΔH using Miedema's formula for transition MHs system shows good agreement with experimental quantities. Meanwhile, Miedema's formula yields fairly reasonable estimates of hydride heats of formation. However, these ΔH are not true heats of hydrides formation, just only provide a means of comparison. Inspired by Miedema's formula, analogously, the ΔH value of the $TiCr_{2-x}Mn_x$ alloys can calculate by the heat released when H atoms occupy the tetrahedron interstices. Here, eight H atoms were stored in the A_2B_2 tetrahedral interstitial of Ti_4Cr_8 cell to ensure that the state of hydride for all $TiCr_{2-x}Mn_x$ (x = 0, 0.25, 0.5, 0.75, 1) were located on the hydrogen absorption/desorption plateau. In particular, a specific number of Ti–Ti–Cr–Cr and Ti–Ti–Cr–Mn tetrahedral interstitials occupied by H atoms were used to simulate hydrides of different Mn content, e.g. eight $6h_1$-type Ti–Ti–Cr–Cr tetrahedral interstitials occupied by H atoms to simulate $TiCr_2H_2$, while four $6h_1$-type Ti–Ti–Cr–Cr and four $6h_1$-type Ti–Ti–Cr–Mn tetrahedral interstitials occupied by H atoms to simulate $TiCr_{1.5}Mn_{0.5}H_2$. The E_{sol} were calculated for specified metal hydrides, such as $TiCr_2H_2$, $TiCr_{1.75}Mn_{0.25}H_2$, $TiCr_{1.5}Mn_{0.5}H_2$, $TiCr_{1.25}Mn_{0.75}H_2$

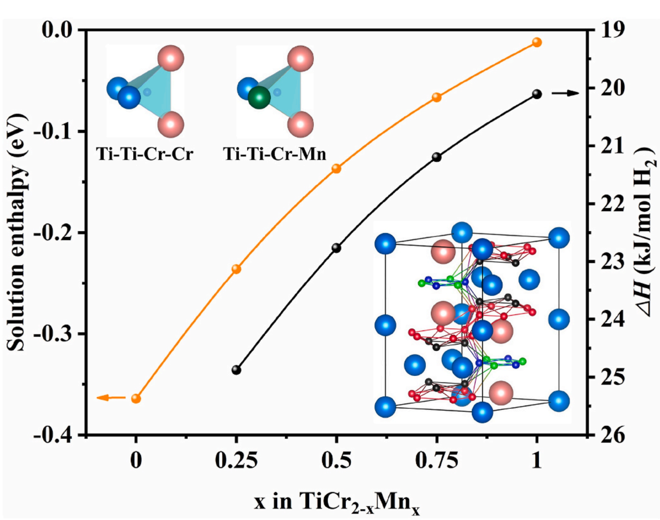

Fig. 6. The relationship between ΔH and.E_{sol}

and $TiCrMnH_2$. As shown in Fig. 6, the E_{sol} values monotonically increase from −0.3642 eV for $TiCr_2H_2$ to −0.0123 eV for $TiCrMnH_2$, indicates that the heat released during hydride generation decrease with the increase of Mn content, which shows good agreement with the change of ΔH values of the $TiCr_{2-x}Mn_x$ detected in experiment. The relationship between E_{sol} and ΔH can be regarded as a reference for developing multicomponent AB_2-type alloy design.

3.4. Hydrogen dissociation and diffusion kinetics

3.4.1. H_2 dissociation on (1 1 0) surface

As mentioned in **Section 3.1**, for $TiCr_{2-x}Mn_x$ (x = 0, 0.25, 0.5, 0.75, 1) alloys, the Mn substitute for Cr in order of fractional coordinates (1, 0, 0.5), (1, 0, 1), (0.83, 0.17, 0.25), (0.17, 0.83, 0.75), indicate the substitution sites are all located on (1 1 0) plane. Therefore, the (1 1 0) surface was selected as the exposed surface, due to it contains Ti, Cr and Mn atoms at the same time. As shown in Fig. S5 (a), the (1 1 0) surface was cleaved and slab model of (1 1 0) surface with 2–6 cells (4–12 atomic layers) and 15 Å vacuum layer was geometrically relaxed, respectively. Fig. S5 (b) compares the E_{surf} of the slab model which upper two and three atomic layers were as the relaxation layer. As shown, the E_{surf} of these two slab models tend to stabilize at 0.1831and 0.1830 eV/$Å^2$ as the thickness of the slab model increases in general. Therefore, the eight layers slab model including three relaxation layers was utilized for the adsorption model.

For the adsorption model of $TiCr_2$ (1 1 0) surface, three kinds of possible adsorption sites, including hollow site (HS), top site (TS) and bridge site (BS), are considered as shown in Fig. S6. Here, one H atom was placed on these adsorption sites and their adsorption energy (E_{ads}) for H atom were calculated, as summarized in Table S4. Obviously, hydrogen atoms can be adsorbed stably at all these positions, and their vertical distances from the surface are between 1.14 and 1.75 Å after adsorption. Among them, the Ti2–Cr2–Cr3 HS shows the strongest E_{ads} of −1.1758 eV, which implies that H prefers to adsorb at the Ti2–Cr2–Cr3 HS. In addition, as shown in Fig. S6 (a) and Table S4, the Cr2 and/or Cr3 were substituted by Mn atoms to form Ti2–Mn2–Cr3, Ti2–Cr2–Mn3 and Ti2–Mn2–Mn3 HS of $TiCr_{2-x}Mn_x$ alloys, respectively. The E_{ads} of Ti2–Mn2–Cr3, Ti2–Cr2–Mn3 and Ti2–Mn2–Mn3 HS increases to −0.9529, −0.9013 and −0.7937 eV, respectively, indicates the addition of Mn has a negative effect on the adsorption of H atom on alloy surface. Furthermore, as shown in Fig. S7 (b) and Table S4, the value of E_{ads} of Cr2–Cr3 BS is also greater than that of Mn2–Cr3, Cr2–Mn3 and Mn2–Mn3 BS, which once again confirms this conclusion.

After that, as shown in Fig. S8, the interactions between H_2 and the most stable position (Ti2–Cr2–Cr3 HS) of $TiCr_2$ (1 1 0) surface were studied, where the initial configuration of H_2 was first divided into parallel a, b and c axis to the (1 1 0) surface, respectively. Based on the distance of H atoms adsorb stably at the surface, the distance between H_2 molecule to the surface ($d_{H2\text{-}surf}$) was set as 1.75 Å. After optimization, as listed in Table S5, the H–H bonds all break and bonds length ($d_{H\text{-}H}$) increase from 0.7509 Å to 2.6455–2.9244 Å, which indicates there is a strong interaction between alloy surface and H_2 at this distance. And it's a stable chemisorption. Compared with the configuration of H_2 parallel a and b, H_2 is preferentially adsorbed in a perpendicular manner because it has the lowest E_{ads} with −2.1890 eV. There is a good consistency with the reported in the literature [27].

In the same way, the Cr2 was substituted by Mn atom to form Ti2–Mn2–Cr3 HS of $TiCr_{2-x}Mn_x$ alloys. Then, the H_2 is set vertically at Ti2–Mn2–Cr3 HS and the E_{ads} after the optimization were also summarized in Table S5. Although H_2 dissociates at Ti2–Mn2–Cr3 HS, the value of E_{ads} increases with the addition of Mn atoms from −2.1890 to −1.7881eV. This once again confirms that the substitution of Cr by Mn is unfavorable to the surface adsorption of H_2.

The above E_{ads} calculation results indicate that the most stable chemisorption of vertical H_2 occurs at Ti2–Cr2–Cr3 HS. Besides, the stable physical adsorption model was optimized by gradually increasing in the vertical distance ($d_{H2\text{-}surf}$) between the H_2 to surface. As listed in Table S5, when the distance between the H_2 and surface reaches ~3.8 Å, H_2 is stable adsorbed to Ti2–Cr2–Cr3 HS. The H–H bond length ($d_{H\text{-}H}$) is ~0.7527–0.7530 Å, which is almost equal to our calculation for that of free H_2 (0.7509 Å), indicating that H_2 is not dissociated. The H_2 molecule is physically adsorbed at Ti2–Cr2–Cr3 and Ti2–Mn2–Cr3 HS with an adsorption energy of −0.1039eV and −0.025eV, respectively.

Based on the above stable physisorption model and chemisorption model at Ti2–Cr2–Cr3 HS, the possible dissociation path and energy barrier of H_2 at the stable adsorption site of $TiCr_2$ (1 1 0) surface were simulated by CI-NEB method. The energy barrier and structure diagrams of H_2 dissociation at Ti2–Cr2–Cr3 HS are plotted in Fig. 7 (a). For H_2 dissociation reaction, the initial reactant H_2 was firstly physisorption at a distance of 3.95 Å. Then, as the transition state model moves closer to the surface, the bond length of H–H bond gradually becomes longer until it breaks. Finally, two isolated H atoms were formed. This dissociation step needed to overcome an energy barrier of 1.80 eV, meanwhile release energy being −2.09 eV. The H–H distance spread from 0.75 Å to 2.92 Å.

In the same way, the energy barrier and structure diagrams of H_2 dissociation at the Ti2–Mn2–Cr3 HS of $TiCr_{2\text{-}x}Mn_x$ alloys are plotted in Fig. 7 (b). The distance of initial H_2 is 3.83 Å to Ti2–Mn2–Cr3 HS. Then, two isolated hydrogen atoms were formed via the dissociation of H_2. Finally, the energy barrier of the dissociation of H_2 at the Ti2–Mn2–Cr3 increases slightly to −1.87 eV. This once again confirms that the substitution of Cr by Mn is unfavorable to the surface adsorption and dissociation of H_2.

3.4.2. H atom diffusion kinetics in the bulk alloys

After that, the H atom adsorbed on the surface diffuses into the subsurface driven by hydrogen pressure. The results of E_{sol} of $TiCr_2$–H system indicate that $6h_1$ tetrahedral interstice is the most stable site for the occupation of H atom in the bulk of $TiCr_2$ alloy. Therefore, the diffusion kinetics of H atoms from the surface Ti2–Cr2–Mn2 HS to the subsurface $6h_1$ tetrahedral interstice was calculated by CI-NEB approach. As shown in Fig. 8 (a), for $TiCr_2$ alloy, H atom must overcome an energy barrier of 1.38 eV to diffuse from the surface into the bulk. Meanwhile, the heat equivalent to 0.90 eV is released when H atom enters the bulk from adsorption state to form hydride, indicating that the total energy of hydride decreases, which is consistent with the conclusion of thermodynamics results. After Mn is substituted for Cr to form Mn substituted surface, as shown in Fig. 8 (b), the energy barrier of H atom increases to 1.52 eV. However, because the enthalpy value of $TiCr_{2\text{-}x}Mn_x$ is lower than that of $TiCr_2$, only 0.82 eV heat is released when hydride formed.

Then, H atom at the subsurface further diffuses from $6h_1$ to the closest neighboring tetrahedral interstices. Fig. S9 shows the diffusion energy barrier of an H atom from $6h_1$ tetrahedral interstice diffuses to $6h_2$, $12k_2$, $6h_1$, $12k_1$, 24l and 4f tetrahedral interstice. Among them, the diffusion path of $6h_1$ to $6h_2$ shows the lowest diffusion barrier with 0.21 eV, which indicated the path of $6h_1$ to $6h_2$ is favorable in the bulk $TiCr_2$ alloy. In addition, the path of $6h_1$ to $6h_2$ in hydride with different H contents were compared. As shown in Figs. S10 and S11, the volume of hydride expands linearly when H atoms are absorbed into 24l tetrahedral interstices. And the cell volume $6h_1$ and $6h_2$ tetrahedron increase first with the increase of cell volume of hydride, then decrease due to the extrusion of the neighboring 24l tetrahedron interstices occupied by H atoms. The CI-NEB kinetics simulation results of H diffusion from $6h_1$–$6h_2$ indicate that the increase in the volume of tetrahedral interstice is conducive to the diffusion of H atoms in hydride, which decrease from 0.20 to 0.17eV. However, as the concentration of H in the hydride continues to increase, the tetrahedron is squeezed and the diffusion of H is blocked. This is consistent with the analysis results of hydrogen absorption rates at different hydrogen absorption stages by Mintz et al. [56].

In addition, the diffusion properties of H atoms in the bulk of $TiCr_{2\text{-}x}Mn_x$ alloys were also studied by substituting Cr by Mn in $6h_1$ and $6h_2$ tetrahedral interstice. Thus, two diffusion types from $6h_1$–$6h_2$ tetrahedral interstice after substitution were study, namely Ti–Ti–Cr–Cr → Ti–Ti–Cr–Mn and Ti–Ti–Cr–Mn → Ti–Ti–Cr–Mn, as shown in Fig. 8 (c). The type of Ti–Ti–Cr–Cr to Ti–Ti–Cr–Cr represents the lowest diffusion barrier with 0.21 eV among them. The type of Ti–Ti–Cr–Mn to Ti–Ti–Cr–Mn represents the highest diffusion barrier with 0.29 eV. Obviously, the addition of Mn increases the diffusion barrier of H atom in the bulk of $TiCr_{2\text{-}x}Mn_x$ alloys.

Fig. 8 (d) shows the normalized isothermal hydrogen absorption curves of $TiCr_{2\text{-}x}Mn_x$ (x = 0, 0.25, 0.5, 0.75, 1) alloys at 30 °C under 30 MPa H_2. It should be noted that the hydrogen absorption kinetics is very fast, and when the system pressure begins to decrease monotonously, the amount of hydrogen absorption has reached more than half. For the $TiCr_2$ alloy, 90% hydrogen absorption capacity is reached in 36.7 s, whereas with the addition of Mn, $TiCr_{0.5}Mn_{0.5}$ is in 70.6 s. With the Mn content continues to increase to x = 1, the total time of 90% hydrogen absorption increases to 160.7 s. There is a good agreement with the results of H atom diffusion kinetics in the bulk alloys by DFT.

4. Conclusions

In this work, the structural stability, hydrogen storage

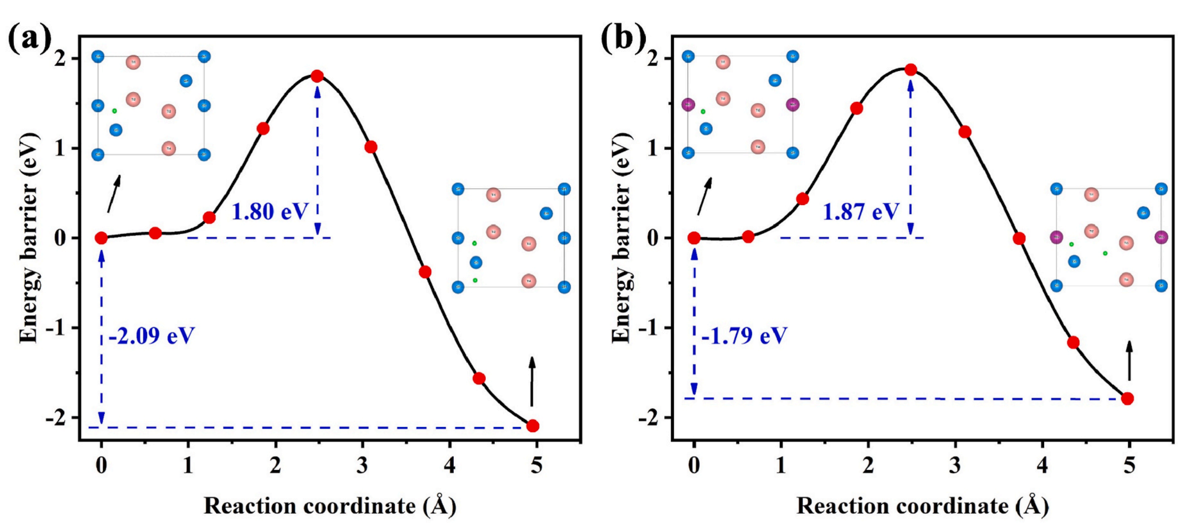

Fig. 7. Dissociation of H_2 molecules on Ti3–Cr2–Cr3 HS of $TiCr_2$ (1 1 0) surface (a) and Ti3–Mn2–Cr3 HS of $TiCr_{2\text{-}x}Mn_x$ (1 1 0) surface (b).

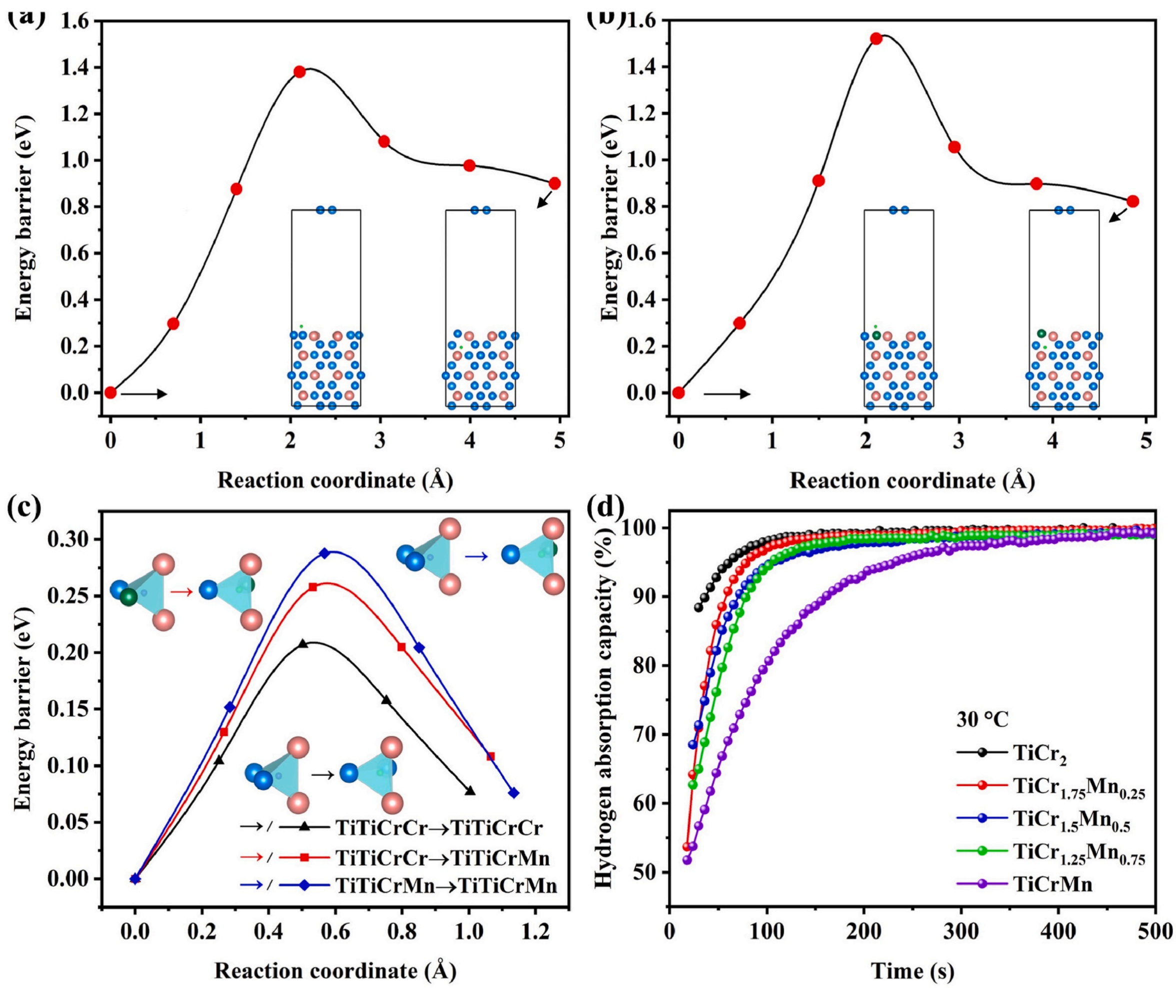

Fig. 8. Calculated diffusion energy barriers of an H atom from surface to $TiCr_2$ bulk (a) and $TiCr_{2-x}Mn_x$ bulk (b), H atom diffuses from $6h_1$–$6h_2$ tetrahedral interstice (c) and the normalized isothermal hydrogen absorption curves of $TiCr_{2-x}Mn_x$ alloys (d).

thermodynamic and kinetic performances of $TiCr_{2-x}Mn_x$ (x = 0, 0.25, 0.5, 0.75, 1) alloys have been studied by using a combination of first principles methods and experiments. The $TiCr_{2-x}Mn_x$ alloys are energetically favorable stable according to the formation enthalpy analysis, and Mn atoms can optionally substitute for the Cr sites. In addition, the solution enthalpy of interstitial H atom decreases with the Mn addition, which provides a reference for predicting the trend of enthalpy of alloys. Finally, the kinetics simulation show that the addition of Mn is unfavorable to the dissociation of H_2 on the surface and the diffusion of H atoms in the bulk alloys. On the other hand, the experimental investigates were carried out under the guidance of calculated results. With the addition of Mn, the alloys maintain a single C14 structure. And the hydrogen storage capacity increases firstly, then decreases due to the decrease of cell volume. Specially, the derived reaction enthalpy of $TiCr_{2-x}Mn_x$ hydride decrease, which is consistent with the enthalpy trend predicted by solution enthalpy. There is also a good agreement with the DFT results of hydrogen dissociation and diffusion kinetics in the bulk alloys, which the TiCrMn alloy takes 124 s longer than the original $TiCr_2$ alloy when 90% hydrogen absorption capacity is reached. The analysis above provides a reference for adding alloying elements with the similar properties as Mn to further improve the plateau pressure, so as to achieve the application of hydrogen compression. In addition, the kinetics of TiCrMn alloy is need to further improve by more modification.

CRediT authorship contribution statement

Wenbin Jiang: conceived the concept of this work and designed experiments, carried out the experiments and calculations with assistance from, and, writed original draft. **Changchun He:** writed original draft, and. **Xiaobao Yang:** writed original draft, revised original draft. **Xuezhang Xiao:** revised original draft, and. **Liuzhang Ouyang:** conceived the concept of this work and designed experiments, carried out the supervision of research, revised original draft. **Min Zhu:** carried out the supervision of research.

Declaration of competing interest

The authors declare that they have no known competing financial interests or personal relationships that could have appeared to influence the work reported in this paper.

Acknowledgements

This work was financially supported by the National Key Research and Development Program of China (No. 2019YFB1505101), the Foundation for Innovative Research Groups of the National Natural Science Foundation of China (No. NSFC51621001).

Appendix A. Supplementary data

Supplementary data to this article can be found online at https://doi.

org/10.1016/j.renene.2022.07.113.

References

[1] Z. Chen, Z. Ma, J. Zheng, X. Li, E. Akiba, H. Li, Perspectives and challenges of hydrogen storage in solid-state hydrides, Chin. J. Chem. Eng. 29 (2021) 1–12.
[2] Y. Wang, X. Chen, H. Zhang, G. Xia, D. Sun, X. Yu, Heterostructures built in metal hydrides for advanced hydrogen storage reversibility, Adv. Mater. 32 (31) (2020), 2002647.
[3] S.E. Hosseini, M.A. Wahid, Hydrogen production from renewable and sustainable energy resources: promising green energy carrier for clean development, Renew. Sustain. Energy Rev. 57 (2016) 850–866.
[4] S. Liu, J. Liu, X. Liu, J. Shang, L. Xu, R. Yu, J. Shui, Hydrogen storage in incompletely etched multilayer Ti_2CT_x at room temperature, Nat. Nanotechnol. 16 (3) (2021) 331–336.
[5] L. Ouyang, J. Jiang, K. Chen, M. Zhu, Z. Liu, Hydrogen production via hydrolysis and alcoholysis of light metal-based materials: a review, Nano-Micro Lett. 13 (1) (2021) 1–30.
[6] M.V. Lototskyy, V.A. Yartys, B.P. Tarasov, M.W. Davids, R.V. Denys, S. Tai, Modelling of metal hydride hydrogen compressors from thermodynamics of hydrogen – metal interactions viewpoint: Part I. Assessment of the performance of metal hydride materials, Int. J. Hydrogen Energy 46 (2) (2021) 2330–2338.
[7] M.V. Lototskyy, V.A. Yartys, B.P. Tarasov, R.V. Denys, J. Eriksen, M. S. Bocharnikov, S. Tai, V. Linkov, Modelling of metal hydride hydrogen compressors from thermodynamics of hydrogen – metal interactions viewpoint: Part II. Assessment of the performance of metal hydride compressors, Int. J. Hydrogen Energy 46 (2) (2021) 2339–2350.
[8] Z. Peng, Q. Li, L. Ouyang, W. Jiang, K. Chen, H. Wang, J. Liu, Z. Li, S. Wang, M. Zhu, Overview of hydrogen compression materials based on a three-stage metal hydride hydrogen compressor, J. Alloys Compd. 895 (2022), 162465.
[9] P. Zhou, Z. Cao, X. Xiao, R. Li, Z. Liang, H. Zhang, L. Zhan, Z. Li, L. Jiang, L. Chen, Dynamically staged phase transformation mechanism of Co-containing rare earth-based metal hydrides with unexpected hysteresis amelioration, ACS Appl. Energy Mater. (2022).
[10] S. Nayebossadri, D. Book, Development of a high-pressure Ti-Mn based hydrogen storage alloy for hydrogen compression, Renew. Energy 143 (2019) 1010–1021.
[11] J. Li, X. Jiang, Z. Li, L. Jiang, X. Li, High-pressure hydrogen storage properties of $Ti_xCr_{1-y}Fe_yMn_{1.0}$ alloys, Int. J. Energy Res. 43 (11) (2019) 5759–5774.
[12] J. Li, Y. Guo, X. Jiang, S. Li, X. Li, Hydrogen storage performances, kinetics and microstructure of $Ti_{1.02}Cr_{1.0}Fe_{0.7-x}Mn_{0.3}Al_x$ alloy by Al substituting for Fe, Renew. Energy 153 (2020) 1140–1154.
[13] C. Qin, C. Zhou, L. Ouyang, J. Liu, M. Zhu, T. Sun, H. Wang, High-pressure hydrogen storage performances of $ZrFe_2$ based alloys with Mn, Ti, and V addition, Int. J. Hydrogen Energy 45 (16) (2020) 9836–9844.
[14] C. Qin, H. Wang, J. Liu, L. Ouyang, M. Zhu, Tuning hydrogen storage thermodynamic properties of $ZrFe_2$ by partial substitution with rare earth element Y, Int. J. Hydrogen Energy 46 (35) (2021) 18445–18452.
[15] Q. Li, Z. Peng, W. Jiang, L. Ouyang, H. Wang, J. Liu, M. Zhu, Optimization of Ti-Zr-Cr-Fe alloys for 45MPa metal hydride hydrogen compressors using orthogonal analysis, J. Alloys Compd. 889 (2022), 161629.
[16] Y. Osumi, H. Suzuki, A. Kato, K. Oguro, T. Sugioka, T. Fujita, Hydrogen storage properties of $Ti_{1+x}Cr_{2-y}Mny$ alloys, J. Less Common Met. 89 (1983) 257–262.
[17] Z. Yao, Z. Liang, X. Xiao, J. Qi, J. He, X. Huang, H. Kou, W. Luo, C. Chen, L. Chen, Achieving excellent cycle stability in Zr–Nb–Co–Ni based hydrogen isotope storage alloys by controllable phase transformation reaction, Renew. Energy 187 (2022) 500–507.
[18] O. Beeri, D. Cohen, Z. Gavra, M.H. Mintz, Sites occupation and thermodynamic properties of the $TiCr_{2-x}Mn_x$–H_2 ($0 \le x \le 1$) system: statistical thermodynamics analysis, J. Alloys Compd. 352 (1–2) (2003) 111–122.
[19] D. Cohen, O. Beeri, Z. Gavra, J.R. Johnson, M.H. Mintz, Thermodynamic characterization and statistical thermodynamics of the TiCrMn–H (D) system, J. Alloys Compd. 299 (2000) 217–226.
[20] G. Bruzzone, M. Ferretti, G. Olcese, Hydrogen absorption by $TiCr_{2-x}Fe_x$ alloys, J Zeitschrift für Physikalische Chemie 145 (1–2) (1985) 61–69.
[21] Z. Nong, J. Zhu, X. Yang, Y. Cao, Z. Lai, Y. Liu, W. Sun, First-principles calculations of the stability and hydrogen storage behavior of C14 Laves phase compound TiCrMn, Solid State Sci. 32 (2014) 1–7.
[22] F. Li, J. Zhao, L. Sun, Substitution effects on the hydrogen storage behavior of AB_2 alloys by first principles, Frontiers of Physics 6 (2) (2011) 214–219.
[23] G. Kresse, J. Hafner, Ab initio molecular dynamics for liquid metals, Phys. Rev. B Condens. Matter 47 (1) (1993) 558–561.
[24] G. Kresse, J. Furthmüller, Efficient iterative schemes for ab initio total-energy calculations using a plane-wave basis set, J Physical review B 56 (16) (1996), 11169.
[25] R. Murugeswari, A.M.F. Benial, R. Rajeswarapalanichamy, Structural, elastic, magnetic and electronic properties of TiX_2(X = Cr, Mn) alloys, Int. J. Mod. Phys. B 33 (12) (2019).
[26] W. Luo, L. Wan, G. Li, T. Gao, Adsorption and dissociation behavior of H2 on PuH2 (100), (110) and (111) surfaces: a density functional theory+U study, RSC Adv. 10 (33) (2020) 19576–19586.
[27] J. Qin, C. Hao, D. Wang, F. Wang, X. Yan, Y. Zhong, Z. Wang, C. Hu, X. Wang, Investigation of adsorption, dissociation, and diffusion properties of hydrogen on the V (100) surface and in the bulk: a first-principles calculation, J. Adv. Res. 21 (2020) 25–34.
[28] N. Liu, S. Zhou, Gas adsorption on monolayer blue phosphorus: implications for environmental stability and gas sensors, Nanotechnology 28 (17) (2017), 175708.
[29] J. Qin, Z. Wang, D. Wang, F. Wang, X. Yan, Y. Zhong, C. Hu, H. Zhou, First-principle investigation of hydrogen solubility and diffusivity in transition metal-doped vanadium membranes and their mechanical properties, J. Alloys Compd. 805 (2019) 747–756.
[30] L. Liu, L. Chen, X. Xiao, C. Xu, J. Sun, S. Li, H. Ge, L. Jiang, Influence of annealing treatment on the microstructure and hydrogen storage performance of $Ti_{1.02}Cr_{1.1}Mn_{0.3}Fe_{0.6}$ alloy for hybrid hydrogen storage application, J. Alloys Compd. 636 (2015) 117–123.
[31] B.H. Toby, R.B. Von Dreele, GSAS-II: the genesis of a modern open-source all purpose crystallography software package, J. Appl. Crystallogr. 46 (2) (2013) 544–549.
[32] M.S. Ali, M. Roknuzzaman, R. Parvin, A.K.M.A. Islam, K. Ostrikov, Electronic, optical and thermal properties of $TiCr_2$ and $TiMn_2$ by ab initio simulations, Int. J. Mod. Phys. B 29 (31) (2015), 1550223.
[33] V. Svechnikov, M.Y. Teslyuk, A. Kocherzhinsky, V. Petkov, E. Dabizha, Three modifications of $TiCr_2$, Dopov. Akad. Nauk. Ukr. RSR 32 (1970) 837–842.
[34] C. He, J. Liao, S. Qiu, Y. Zhao, X. Yang, Biased screening for multi-component materials with structures of alloy generation and recognition (SAGAR), Comput. Mater. Sci. 193 (2021), 110386.
[35] C. He, S. Qiu, J. Yu, J. Liao, Y. Zhao, X. Yang, Atom classification model for total energy evaluation of two-dimensional multicomponent materials, J. Phys. Chem. A 124 (22) (2020) 4506–4511.
[36] X. Yang, J. Ni, Ground states of adsorbates on single-walled carbon nanotubes, Phys. Rev. B 67 (19) (2003), 195403.
[37] G. Trimarchi, A.J. Freeman, A. Zunger, Predicting stable stoichiometries of compounds via evolutionary global space-group optimization, Phys. Rev. B 80 (9) (2009), 092101.
[38] Z. Liang, Z. Yao, R. Li, X. Xiao, Z. Ye, X. Wang, J. Qi, J. Bi, X. Fan, H. Kou, W. Luo, C. Chen, L. Chen, Regulating local chemistry in ZrCo-based orthorhombic hydrides via increasing atomic interference for ultra-stable hydrogen isotopes storage, J. Energy Chem. 69 (2022) 397–405.
[39] F. Agresti, S. Lo Russo, A. Maddalena, G. Principi, G. Mazzolai, B. Coluzzi, A. Biscarini, F.M. Mazzolai, A. Tuissi, Reaction of hydrogen with the Laves phase (C14) $TiCr_{1.78}$−Mn compounds, Mater. Sci. Eng., A 521–522 (2009) 143–146.
[40] Z. Wang, J. Qin, Q. Hu, D. Wang, F. Wang, Y. Zhong, J. Zhang, H. Zhou, M. Dong, C. Hu, H. Liu, Z. Guo, Theoretical investigation of molybdenum/tungsten-vanadium solid solution alloy membranes: thermodynamic stability and hydrogen permeation, J. Membr. Sci. 608 (2020), 118200.
[41] M.S.C. Mazzoni, R.W. Nunes, S. Azevedo, H. Chacham, Electronic structure and energetics of $B_xC_yN_z$ layered structures, Phys. Rev. B 73 (7) (2006), 073108.
[42] D. Ivey, D. Northwood, Hydrogen site occupancy in AB_2 Laves phases, Journal of Less-Commom Metals 115 (1986) 23–33.
[43] A.R. Merlino, C.R. Luna, A. Juan, M.E. Pronsato, A DFT study of hydrogen storage in $Zr(Cr_{0.5}Ni_{0.5})_2$ Laves phase, Int. J. Hydrogen Energy 41 (4) (2016) 2700–2710.
[44] D.P. Shoemaker, C.B. Shoemaker, Concerning atomic sites and capacities for hydrogen absorption in the AB_2 Friauf-Laves phases, J. Less Common Met. 68 (1) (1979) 43–58.
[45] A. Switendick, Theoretical Studies of Hydrogen in Metals: Current Status and Further Prospects, Sandia Labs., 1978.
[46] J. Qin, Z. Wang, D. Wang, Y. Wu, Y. Zhong, C. Hu, H. Zhou, Dissolution, diffusion, and penetration of H in the group VB metals investigated by first-principles method, Int. J. Hydrogen Energy 44 (55) (2019) 29083–29091.
[47] Z. Li, H. Wang, L. Ouyang, J. Liu, M. Zhu, Achieving superior de-/hydrogenation properties of C15 Laves phase Y-Fe-Al alloys by A-side substitution, J. Alloys Compd. 787 (2019) 158–164.
[48] A. Miedema, The electronegativity parameter for transition metals: heat of formation and charge transfer in alloys, J. Less Common Met. 32 (1) (1973) 117–136.
[49] A. Miedema, R. Boom, F. De Boer, On the heat of formation of solid alloys, J. Less Common Met. 41 (2) (1975) 283–298.
[50] A. Miedema, On the heat of formation of solid alloys. II, J. Less Common Met. 46 (1) (1976) 67–83.
[51] Z. Peng, Q. Li, J. Sun, K. Chen, W. Jiang, H. Wang, J. Liu, L. Ouyang, M. Zhu, Ti-Cr-Mn-Fe-based alloys optimized by orthogonal experiment for 85 MPa hydrogen compression materials, J. Alloys Compd. 891 (2022), 161791.
[52] Z. Cao, L. Ouyang, H. Wang, J. Liu, D. Sun, Q. Zhang, M. Zhu, Advanced high-pressure metal hydride fabricated via Ti–Cr–Mn alloys for hybrid tank, Int. J. Hydrogen Energy 40 (6) (2015) 2717–2728.
[53] V. Charbonnier, H. Enoki, K. Asano, H. Kim, K. Sakaki, Tuning the hydrogenation properties of $Ti_{1+y}Cr_{2-x}Mn_x$ laves phase compounds for high pressure metal-hydride compressors, Int. J. Hydrogen Energy 46 (73) (2021) 36369–36380.
[54] G. Sandrock, A panoramic overview of hydrogen storage alloys from a gas reaction point of view, J. Alloys Compd. 293–295 (1999) 877–888.
[55] W. Jiang, C. Tan, J. Huang, L. Ouyang, M. Chen, D. Min, C. Liao, R. Tang, M. Zhu, Influence of Sm doping on thermodynamics and electrochemical performance of AB_{5+z} alloys in low-temperature and high-power Ni-metal hydride batteries, J. Power Sources 493 (2021), 229725.
[56] M.H. Mintz, Y. Zeiri, Hydriding kinetics of powders, J. Alloys Compd. 216 (2) (1995) 159–175.